

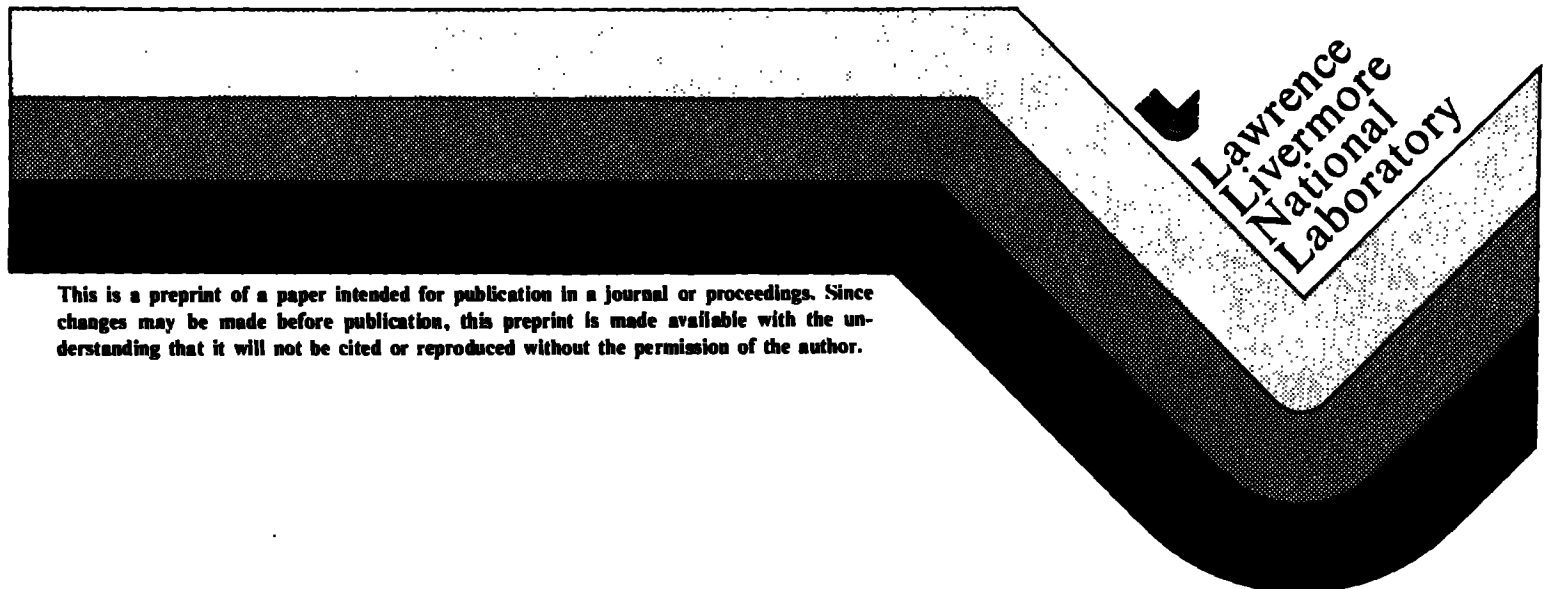
UCRL-93639
PREPRINT

THE BALLISTIC FLIGHT OF A PROJECTILE
WITH TWO PRECESSIONAL MODES

Thomas Morgan

This paper was prepared for submittal to
AIAA 24th Aerospace Sciences Meeting
Reno, Nevada
January 6-9, 1986

November 21, 1985



This is a preprint of a paper intended for publication in a journal or proceedings. Since changes may be made before publication, this preprint is made available with the understanding that it will not be cited or reproduced without the permission of the author.

DISCLAIMER

This document was prepared as an account of work sponsored by an agency of the United States Government. Neither the United States Government nor the University of California nor any of their employees, makes any warranty, express or implied, or assumes any legal liability or responsibility for the accuracy, completeness, or usefulness of any information, apparatus, product, or process disclosed, or represents that its use would not infringe privately owned rights. Reference herein to any specific commercial products, process, or service by trade name, trademark, manufacturer, or otherwise, does not necessarily constitute or imply its endorsement, recommendation, or favoring by the United States Government or the University of California. The views and opinions of authors expressed herein do not necessarily state or reflect those of the United States Government or the University of California, and shall not be used for advertising or product endorsement purposes.

The Ballistic Flight of a Projectile With Two Precessional Modes

Thomas Morgan*,**
Lawrence Livermore National Laboratory
Livermore, California

Abstract

Rapidly spinning projectiles with infinite rotational symmetry display a high degree of physical correspondence to a classical gyroscope. As with a gyroscope, such projectiles show two precessional modes, one of which will always be in evidence during a flight. Aeroballistic theory provides, additionally, for two simultaneously excited nutational modes, with sinusoidal frequencies close to, but not exactly coincident with, the precessional angular velocities. The combination of these two orthonormal rotations gives rise to complex pitching and yawing motion, which can be substantially different than the motion predicted by aeroballistic theory alone. Results from a numerical integration of the equations of motion in their most general form illustrate these differences.

Nomenclature

A	= reference area = S
A_{lp}	= $1/2\rho S l^2 V C_{lp}$
A_{pa}	= $1/2\rho S l^2 V [C_{mpa} + (I_R/ml^2)C_{la}]$
A_q	= $1/2\rho S l^2 V [C_{ma} - (I_T/ml^2)C_{la}]$
A_a	= $1/2\rho S l^2 V^2 C_{ma}$
C_{lp}	= roll damping moment coefficient
C_{la}	= lift force coefficient
C_{mpa}	= Magnus moment coefficient
$C_{m\dot{\alpha}}$	= damping moment coefficient
C_{ma}	= static moment coefficient
$I_M()$	= imaginary part of the indicated variable
I_R	= roll moment of inertia of the projectile
I_T	= transverse moment of inertia of the projectile
l	= reference length
$K_i(i=1,2)$	= constant indeterminate coefficients
m	= mass of the projectile
M_x, M_y, M_z	= components of aerodynamic moment vector in the body-fixed coordinate system
$R_E()$	= real part of the indicated variable
t	= time
V	= magnitude of the velocity vector
Θ	= body nutation angle
Ψ	= body precession angle
$\lambda_i(i=1,2)$	= differential equation complex eigenvalues
ρ	= air density
ϕ	= rotation angle of body-fixed coordinates about z-axis
ω	= angular velocity of the projectile
Ω	= angular velocity of the body-fixed coordinate system with respect to the space fixed coordinate system

Introduction

In atmospheric flight mechanics, the heading angle of a ballistic projectile has traditionally been described with a coordinate system typically well suited to a non-symmetrical body, such as an airplane. In this coordinate system, two natural axes, or degrees of freedom, immediately suggest themselves. They are the "nose-up, nose-down" attitude, known as pitch, and the, "nose-left, nose-right" attitude, known as yaw. A final rotation—the total body-turn angle with respect to Newtonian space, referred to as roll—completes the global, spherical description of position of a projectile in flight.^{1,2} In the absence of rigorous wind-tunnel testing, the atmospheric moments applied to a body and their corresponding non-dimensionalized coefficients are frequently inferred from the oscillatory behavior³ of the body as witnessed along a flight path. Certain other corrections to a projectile's aerodynamic model—such as angle-of-attack nonlinearities and velocity-dependent, aerodynamic coefficient slope reversal—are incorporated into the total equation of motion prior to numerical integration. These corrections, in effect, introduce an empirical match to the expected behavior.

Whenever a body displays a high degree of rotational symmetry (not including cruciform or finned symmetry), a competing coordinate description can also be used to successfully describe a projectile's motion along its trajectory. The second coordinate system relies on an Eulerian rotation sequence resembling a commonly taught derivation of gyroscopic motion. The first rotation is a latitudinal variation, known in classical mechanics as nutation; and the second rotation, one about a longitude, is called precession. A final rotation, spin, describes the rotation of a point on the body from the nutational line of nodes. For simplicity, the gyroscopic coordinate frame may be regarded as the polar form of the aeroballistic coordinate frame.

While it may seem that no advantage accrues from the substitution of one coordinate system for another, the purpose of the following work is to show that certain flight phenomena ascribed to nonlinear or empirical effects may, in fact, be explained with a linear model. The use of a linear model obviates the need for empirical correction factors and thus presents a more rigorous, dynamic description. The difference can be traced to a readily apparent feature of the gyroscopic coordinate frame: namely, that during that phase of motion when the nutation angle does not oscillate, the precessional frequency can have only one of two values, whereas during the oscillatory phase, the precession rate varies sinusoidally about these two values.

During the oscillatory phase, the commonly published analytical solution to the differential equation of motion⁴ does not, in fact, describe the actual flight behavior in the instance of a transition from one of these stable precessional modes to the other. Actually, during most of the period of oscillatory nutation, the precessional frequency exhibits strong oscillations of its own. This behavior contradicts one

* Research Engineer; Member AIAA

** Work performed under the auspices of the U.S. Department of Energy by the Lawrence Livermore National Laboratory under contract No. W-7405-ENG-48.

of the assumptions used in arriving at the analytical solution. The consequence of the failure of this assumption is to limit the total amount of information available to the dynamicist studying the trajectory.

Each aspect of the total body motion will be examined in detail, using the gyroscopic coordinate frame. Numerical solution of the equations of motion will be presented to explain observed flight characteristics.

Theory

With reference to the coordinate system shown in Fig. 1, the total body equations of motion have been derived⁵ from first principles. In Eulerian coordinates using the rotational form of Newton's second law, the inertial expressions are:

$$\Sigma M_x = I_T \ddot{\Theta} + ((I_R - I_T) \dot{\Psi}^2 \cos \Theta + I_R \dot{\Phi} \dot{\Psi}) \sin \Theta, \quad (1a)$$

$$\Sigma M_y = ((2I_T - I_R) \dot{\Psi} \cos \Theta - I_R \dot{\Phi}) \dot{\Theta} + I_T \ddot{\Psi} \sin \Theta, \quad (1b)$$

and

$$\Sigma M_z = I_R (\ddot{\Psi} \cos \Theta - \dot{\Psi} \dot{\Theta} \sin \Theta + \ddot{\Phi}). \quad (1c)$$

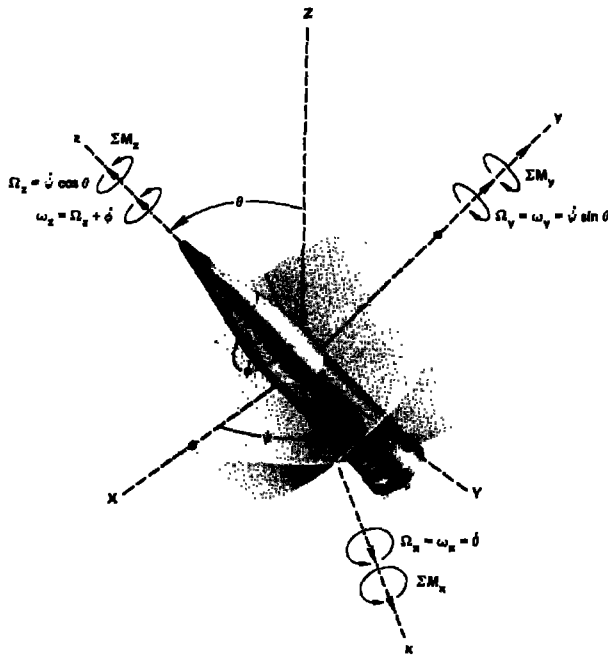


Figure 1.

The applied moments are all aerodynamic and arise from three sources:

1. Linear aerodynamic static moments.

These moments are proportional to the sine of the total nutation angle and are positive (as shown by Fig. 1) when the center of pressure is located ahead of the center of gravity and are negative otherwise. The total expression is

$$M_{ax} = \frac{1}{2} \rho V^2 l A C_{ma} \sin \Theta = A_a \sin \Theta. \quad (2)$$

In the roll axis, the roll damping moment given by Vaughn (Ref. 1) is

$$\begin{aligned} M_{pz} &= \frac{1}{2} \rho V l^2 A C_{lp} (\dot{\Psi} \cos \Theta + \dot{\Phi}) \\ &= A_{lp} (\dot{\Psi} \cos \Theta + \dot{\Phi}). \end{aligned} \quad (3)$$

2. Linear aerodynamic dynamic moments.

Two moments are applied about the y or tangential axis due to the dynamic motions of the shell. They are the Magnus moment, which is the torque applied to a body spinning in a fluid velocity field, written

$$\begin{aligned} M_{py} &= \frac{1}{2} \rho V l^2 A C_{mpa} (\dot{\Phi} + \dot{\Psi} \cos \Theta) \sin \Theta \\ &= A_{pa} (\dot{\Phi} + \dot{\Psi} \cos \Theta) \sin \Theta; \end{aligned} \quad (4)$$

and the dynamic damping moment,

$$M_{qy} = \frac{1}{2} \rho V A l^2 C_{ma} \dot{\Psi} \sin \Theta = A_a \dot{\Psi} \sin \Theta. \quad (5)$$

About the x axis, dynamic damping is given by

$$M_{qx} = \frac{1}{2} \rho V A l^2 C_{ma} \dot{\Theta} = A_a \dot{\Theta}. \quad (6)$$

3. Differential work moments.

Due to the acceleration of the Eulerian-coordinate frame, a differential, aerodynamic torque is applied to the body about all three axes (Ref. 4). Generally, this torque is neglected in the roll axis⁶ but is retained about the x and y axes. Its value in those coordinate directions is

$$M_{qay} = \frac{1}{2} \rho V l^2 A \frac{I_R}{m l^2} C_{la} [\dot{\Phi} + \dot{\Psi} \cos \Theta] \sin \Theta \quad (7)$$

and

$$M_{qax} = \frac{1}{2} \rho V A l^2 \frac{I_T}{m l^2} C_{la} [\dot{\Theta}]. \quad (8)$$

Summing all the moments about the three coordinate axes gives the final equations of motion:

$$\begin{aligned} I_T \ddot{\Theta} - A_q \dot{\Theta} + \\ ((I_R - I_T) \dot{\Psi}^2 \cos \Theta + I_R \dot{\Phi} \dot{\Psi} - A_a) \sin \Theta = 0 \end{aligned} \quad (9a)$$

$$\begin{aligned} ((2I_T - I_R) \dot{\Psi} - I_R \dot{\Phi}) \dot{\Theta} + \\ (I_T \ddot{\Psi} - A_q \dot{\Psi} - A_{pa} (\dot{\Psi} \cos \Theta + \dot{\Phi})) \sin \Theta = 0 \end{aligned} \quad (9b)$$

$$I_R (\ddot{\Psi} + \ddot{\Phi} - \dot{\Psi} \sin \Theta) - A_{lp} (\dot{\Psi} \cos \Theta + \dot{\Phi}) = 0. \quad (9c)$$

When the small-angle approximation is used to linearize the above set equations, they are exactly equivalent to the polar form of the aeroballistic equations (Ref. 6).

For quasi-steady-state precessional motion ($\ddot{\Psi} \approx 0$) a closed-form solution of equations (9a-c) can be found.⁷ The solution is

$$\Theta = K_1 e^{\lambda_1 t} + K_2 e^{\lambda_2 t}, \quad (10)$$

where

$$K_1 = \frac{A(R_E(\lambda_1 - \lambda_2))}{(R_E(\lambda_1 - \lambda_2))^2 + (I_m(\lambda_1 - \lambda_2))^2} - i \frac{A(I_m(\lambda_1 - \lambda_2))}{(R_E(\lambda_1 - \lambda_2))^2 + (I_m(\lambda_1 - \lambda_2))^2}, \quad (11a)$$

$$K_2 = \frac{-B}{R_E(\lambda_1 - \lambda_2)^2 + (I_m(\lambda_1 - \lambda_2))^2} + i \frac{A(I_m(\lambda_1 - \lambda_2))}{(R_E(\lambda_1 - \lambda_2))^2 + (I_m(\lambda_1 - \lambda_2))^2}, \quad (11b)$$

$$\lambda_{1,2} = \frac{-A_q}{2I_T} (1 \pm \tau) \pm \tau \left(\frac{A_{pa} (\dot{\Psi} \cos \Theta + \dot{\Phi})}{I_R} \right) - i \left(\frac{(\dot{\Psi} \cos \Theta + \dot{\Phi})}{2I_T} \right) \left(\frac{I_R}{\tau} \right) (1 \pm 1), \quad (11c)$$

$$\tau = \frac{1}{\sqrt{1 - 1/S_g}} \quad (11d)$$

$$S_g = I_R^2 (\dot{\Psi} \cos \Theta + \dot{\Phi})^2 / 4I_T A_a, \quad (11e)$$

$$A = \dot{\Theta}_o - \Theta_o (R_E(\lambda_2)), \quad (11f)$$

and

$$B = \Theta_o (I_m(\lambda_1 - \lambda_2)^2) - (\dot{\Theta}_o - \Theta_o (R_E(\lambda_1))) (R_E(\lambda_1 - \lambda_2)). \quad (11g)$$

However, efforts to modify the aerodynamic coefficients by matching the analytical solution with observed flight dynamics must *not* be undertaken lightly. For instance, it is a trivial exercise to evaluate the precessional motion when the nutational motion is a known, explicit function. First, the harmonic effects of nutational angle due to the slow frequency are assumed to be small compared to those of the fast frequency. Then, the results are substituted back into the equations of motion [equations (9a-c)].

But if Θ is in fact harmonic, its derivative is also harmonic, which implies [from equation (9b)] that the precession rate must be harmonic. However, the presence of an harmonic precession angle contradicts one of the underlying assumptions ($\dot{\Psi} \approx 0$) that led to the analytical solution. Circumventing this quandary requires knowledge of the exact nature of the precessional modes and the extent of their sinusoidal damping. For this reason, two distinct phases of a projectile flight—oscillatory and non-oscillatory nutational motion—will be treated independently.

Discussion

Non-Oscillatory Motion: Constant Density, Constant Velocity.

If the terms $\ddot{\Psi} = \ddot{\Theta} = \dot{\Theta} = 0$ are substituted into equations (9a) and (b), the expressions reduce to

$$(I_R - I_T) \dot{\Psi}^2 + I_R \dot{\Phi} \dot{\Psi} - A_a = 0 \quad (12a)$$

$$- A_q \dot{\Psi} - A_{pa} (\dot{\Psi} \cos \Theta + \dot{\Phi}) = 0. \quad (12b)$$

Equation (12a) is a simple quadratic with solution

$$\dot{\Psi}_{1,2} = \frac{-I_R \dot{\Phi}}{2(I_R - I_T)} \pm \frac{1}{2(I_R - I_T)} \sqrt{I_R^2 \dot{\Phi}^2 + 4(I_R - I_T) A_a}. \quad (13)$$

Equations 12(a) and 12(b) show precisely the two precessional modes predicted by classical gyroscopic theory.⁸ Now, solving equation (12b) in terms of Θ gives

$$\Theta = \cos^{-1} \left(\frac{-A_q}{A_{pa}} - \frac{\dot{\Phi}}{\dot{\Psi}} \right). \quad (14)$$

When the fast precessional motion is excited, the ratio of the spin rate to the precession rate for most ballistic shells is about 10. This is approximately the same value as for the ratio of aerodynamic coefficients $\frac{A_q}{A_{pa}}$. Hence, a solution for

the argument of the arc cosine is often available, which leads to the observation of a steady-state, circular coning motion at the predicted angle. On the other hand, if slow-mode coning is excited, the ratio of the angular motions is usually greater than 100. Now that the argument of the arc cosine term exceeds 1, no coning motion is possible because the expression is indeterminate. (For the purpose of definition, the existence of fast precession coning at a constant nutation angle will be referred to as "limit cycle motion.")

To display this phenomenon more clearly, a numerical integration of the total equations of motion in their most general form [from equations (9a-c)] has been performed. For illustration purposes, the atmospheric density and the shell velocity are held constant. The initial conditions and applied aerodynamic moments for this simulation are given in Table 1. The results are plotted in Figs. 2 through 5. The following conclusions can be drawn from an examination of these plots:

1. The precession angle oscillates strongly about the mean value of the "slow" precession rate until it reaches the "fast" rate, at which point the oscillations quickly damp to zero. Such motion violates the assumption used to arrive at the analytical solution in this case.

NUTATION ANGLE FOR CONSTANT DENSITY CONSTANT VELOCITY FLIGHT

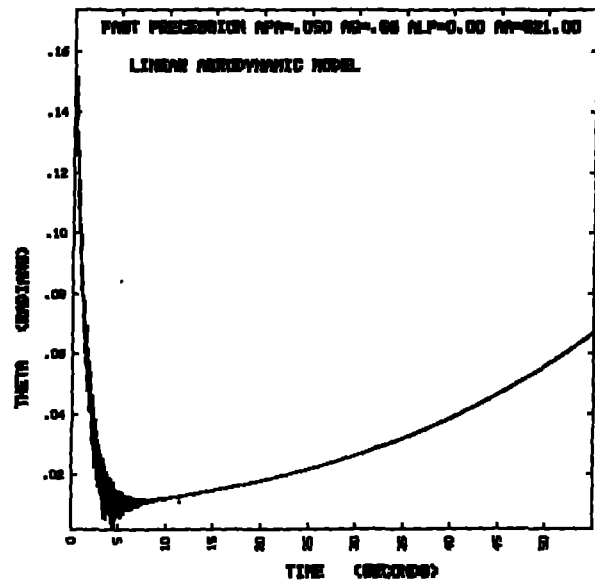


Figure 2.

Table 1. Initial Conditions for Numerical Integration of Transonic CDCV Simulation.

Figures No.	ϕ (rad/sec)	ψ (rad/sec)	I_R (slug-ft ²)	I_T (slug-ft ²)	Θ_0 (Degrees)	$\dot{\Theta}_0$ (rad/sec)	A_q	A_{px}
2-5	618	10	0.1	1.0	10	0.1	0.66	0.050
7-10	618	10	0.1	1.0	10	0.1	0.66	0.025

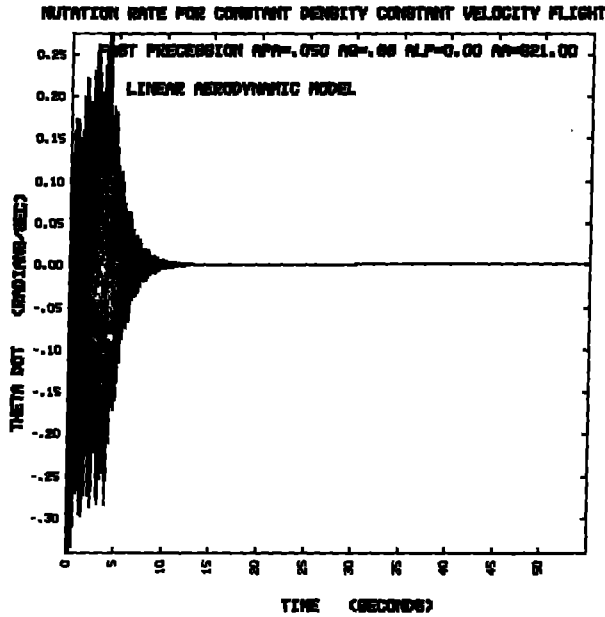


Figure 3.

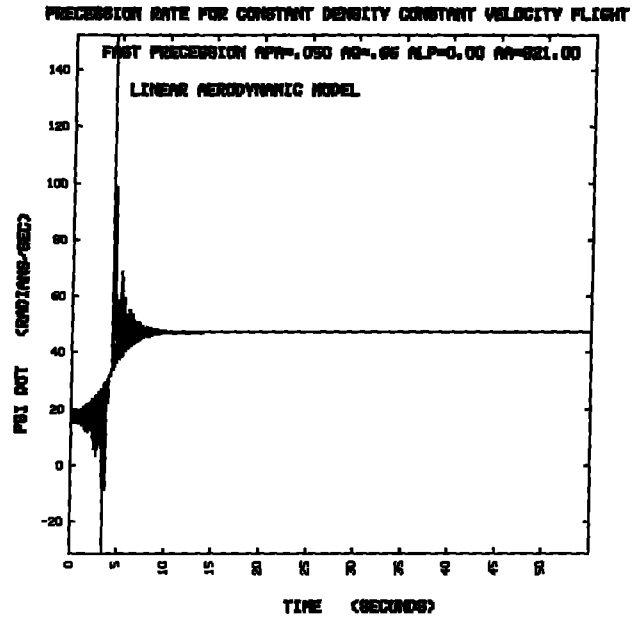


Figure 4.

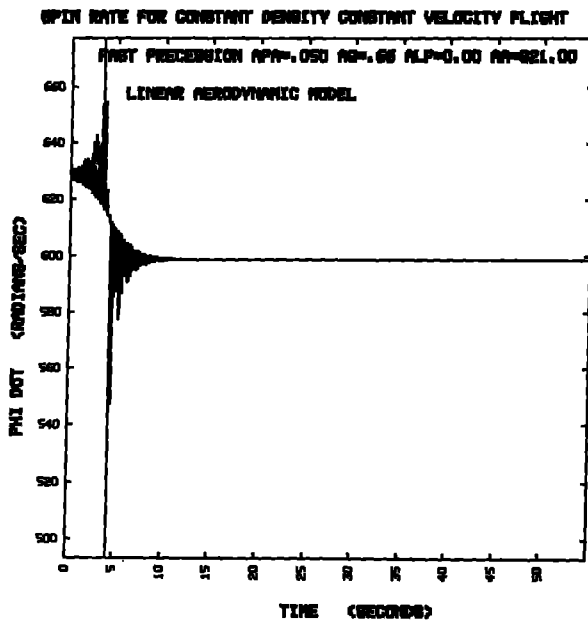


Figure 5.

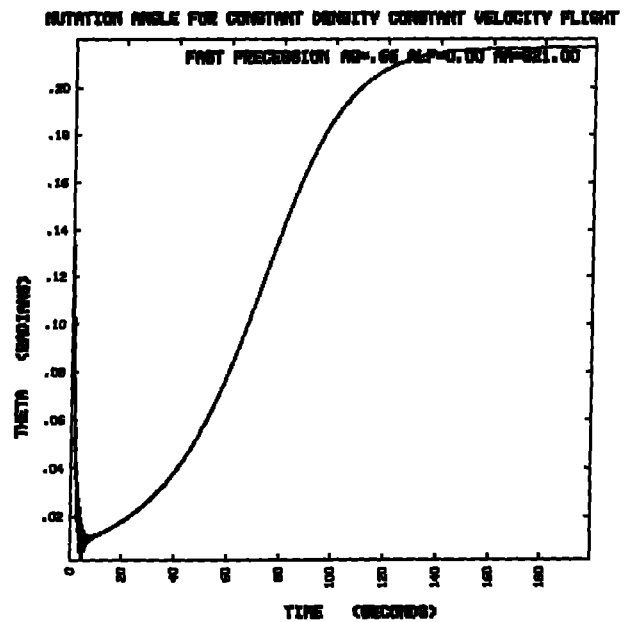


Figure 6.

2. The oscillations in nutation angle damp rather quickly and occupy only a fraction of the usual ballistic flight time. Hence, non-oscillatory motion is the usual condition.
3. The value of final nutation angle is exactly the solution predicted by equation (14) when the motion is allowed to continue to its full development. From the listing of the

results that generated these plots, $\Theta_f = 0.22$ rad., $\dot{\phi}_f = 598$ rad/sec, and $\dot{\psi}_f = 48.9$ rad/sec. The final limit cycle motion is shown in Fig. 6.

Now by manipulation of one of the aerodynamic variables, A_{px} , the reverse can be made to happen. When the initial value of this variable is halved, the plots show a different character. Instead of being undamped in precessional

oscillations, the solution shows moderate damping behavior. But during the non-oscillatory portion of the flight, limit cycle motion is not observed. The results of the numerical integration are given in Figs. 7 through 10.

Predicting that the limit cycle motion of Figs. 2-6 can be achieved with only the linear form of the aerodynamic slope coefficients is impossible given only the aeroballistic formulation. The state of the precessional motion is also required to give the instantaneous nutation history.

Oscillatory Motion: Constant Density, Constant Velocity.

Reexamining Figs. 2 through 9 for those portions of the traces where the nutation angle varies harmonically, the two frequencies predicted by equation (9) are apparent. In

Fig. 2, the mean nutation angle decays rapidly toward zero, while the oscillations about the mean value grow rapidly with time up to about 4 s. At this point, the oscillations begin to damp, but the mean value grows with time. It must be reiterated that these figures use a constant-density, constant-velocity (CDCV) simulation, but nonetheless, damping coefficients appear to be radically different at different points in the flight. An investigation of Fig. 4, on the other hand, shows that, at the same time the transition from damped to undamped nutational oscillations occurred, the precessional motion switched from unstable, slow precession to stable, fast precession.

When the analytical solution is plotted, the motion appears quite at odds with the actual solution, though. In Fig. 11, the sinusoidal envelope of the analytical nutation

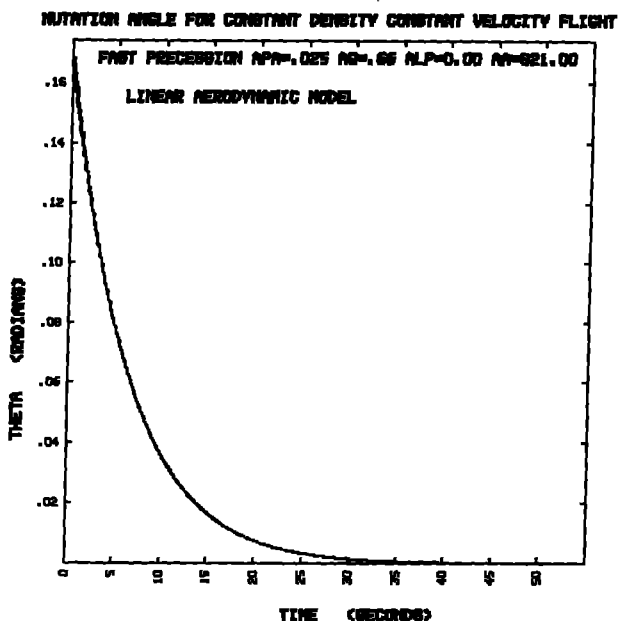


Figure 7.

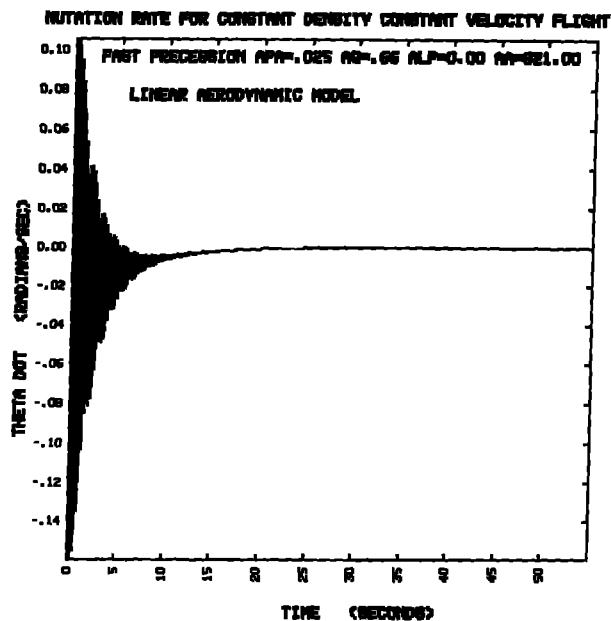


Figure 8.

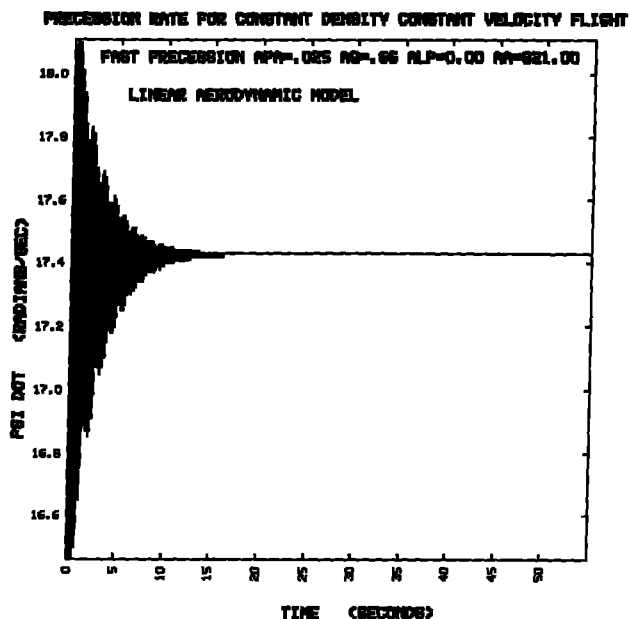


Figure 9.

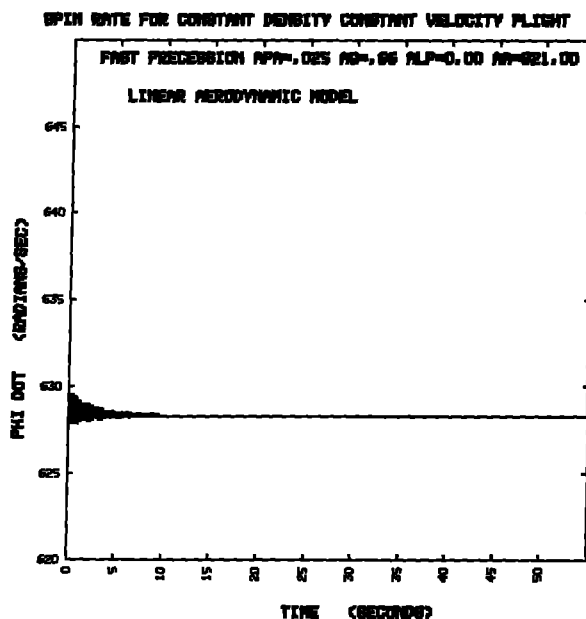


Figure 10.

angle grows exponentially throughout the flight period. Specifically, the analytical solution and the actual solution are widely divergent after the precessional mode transition. At $t = 4.0$ s, when the transition occurs, the constant precession rate assumption is violated, which leads to this significant error in the analytical solution. In the aeroballistic solution, however, nonlinear aerodynamic effects—especially those associated with high angles of attack—are invoked to provide an empirical correction to the observed motion.

Ballistic Flight Simulation.

Incorporating the equations of motion in their most general form into a six degree-of-freedom trajectory model relaxes the assumption of constant density, constant velocity flight. Now, solving the equations of motion numerically gives a true picture of actual flight motion. The prototype aerodynamic model will be drawn from a general Army research shell, the M549, which is a 155-mm (6-in) caliber projectile. Its mass is 2.98 slugs. The aerodynamic model, non-dimensionalized to $\frac{m}{2V}$, is given in Table 2. The initial launch conditions are shown in Table 3. One point should be noted about the aerodynamic model: while all of the aerodynamic coefficients are linear with respect to angle of attack, the Magnus moment coefficient reverses sign at a Mach number of 0.85. The Magnus moment arises from the force applied on a spinning cylinder moving through a viscous fluid at non-zero angle of attack. Its aerodynamic center moves in the

transonic flight regime in a manner similar to the equivalent shift of an airfoil's aerodynamic center from the quarter to the half-chord point at $M = 1.0$. Because of the additional downwash component due to the shell's rotational motion, the transition occurs at a slower velocity. Whether this same

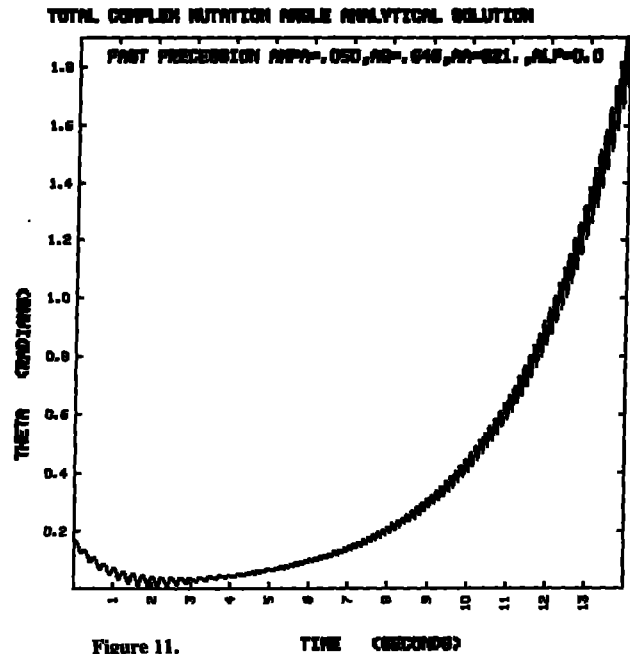


Table 2. M549 Aerodynamic Model (Linear).

Mach Number	C_A	$C_{L\alpha}$	$C_{m\alpha}$	$C_{m\dot{\alpha}}$	$C_{m\dot{\phi}}$	C_{lp}
0.00	0.119	1.495	3.701	-1.10	-1.788	-0.0280
0.45	—	—	—	-1.10	-1.788	—
0.60	—	—	—	-11.00	—	—
0.70	0.119	1.495	3.713	-12.00	-1.788	—
0.80	0.121	1.444	3.988	-16.50	-0.837	—
0.85	0.119	1.444	4.188	—	0.837	—
0.89	0.131	—	—	—	—	—
0.90	—	1.444	4.469	-20.80	1.071	—
0.91	0.147	—	—	—	—	—
0.92	—	1.392	4.548	—	1.192	—
0.93	—	—	—	—	—	-0.0280
0.94	0.173	—	—	—	—	—
0.95	—	1.495	4.698	—	1.432	—
0.96	—	—	—	—	—	-0.0274
0.97	—	1.650	4.435	—	—	—
0.98	0.257	—	—	—	—	—
1.00	0.299	1.805	4.085	-23.50	1.071	-0.0272
1.05	0.328	1.908	3.759	—	1.071	-0.0266
1.10	0.335	2.011	3.736	-25.00	0.957	-0.0260
1.20	0.327	2.114	3.707	—	0.837	—
1.25	—	—	—	—	—	-0.0250
1.30	—	—	—	-26.00	—	—
1.40	0.3090	2.217	3.575	—	0.957	—
1.50	—	—	—	—	—	-0.0238
1.60	0.291	2.269	3.507	-27.00	1.071	—
1.70	—	—	—	—	—	-0.0234
1.90	—	—	—	—	—	-0.0228
2.20	0.237	2.217	3.249	—	1.192	—
3.90	0.176	2.063	3.117	-28.00	1.432	—
4.00	—	—	—	—	—	-0.0216

slope reversal exists at the same velocity for both slow and fast precessional motions is an important, but difficult, question to resolve because the Magnus moment itself is a key index in determining the precessional mode. Also of bearing is the state of the nutational oscillations at the time the shell enters the transonic point.

Two different types of flights will be examined by this simulation: fully supersonic and transonic. Utilizing the trajectory model on a CDC-7600 computer with an integrating algorithm⁹ developed by the Lawrence Livermore National Laboratory's Mathematical Department, the supersonic simulation is presented first in Figs. 12-17. For the initial conditions given in Table 3 and the aerodynamic model shown in Table 2, it is apparent that the normal precessional mode is the slow one. When the nutational variations are examined on an expanded time scale (Fig. 16), the two eigen frequencies of nutational motion are still evident in Θ . By $t = 5.0$ s, all nutational oscillations have decayed to zero; 11 s elapse before the precessional oscillations have damped out. However, as shown in Fig. 17, the Mach number does not approach the point where the Magnus coefficient reverses slope, at $t = 5.0$ s indicating that the nutational damping is *not* due to nonlinearities in the aerodynamic model. The other point of interest is that there is a very slight difference between the frequencies of Ψ and those of Θ . Numerically this difference is the same as that between the nutational eigen frequencies predicted by equation (9) and the steady-state precessional modes predicted by equation (13).

The difference leads to a beat frequency in the modulation envelope of Ψ . In Newtonian space, this beat frequency can be thought of as the slow rotation of the minor axis of an ellipse resulting from the combination of nutation and precession oscillations at almost, but not exactly, the same frequency.

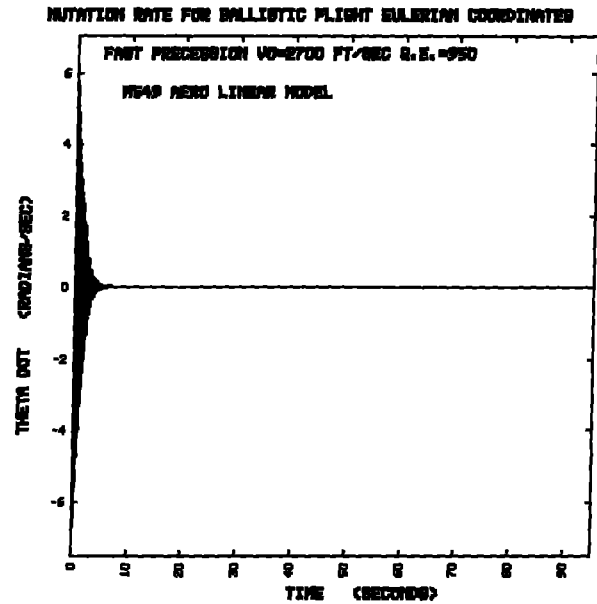


Figure 13.

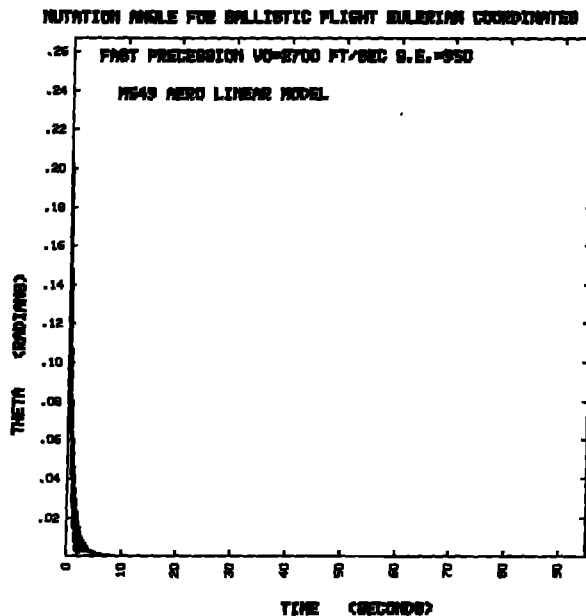


Figure 12.

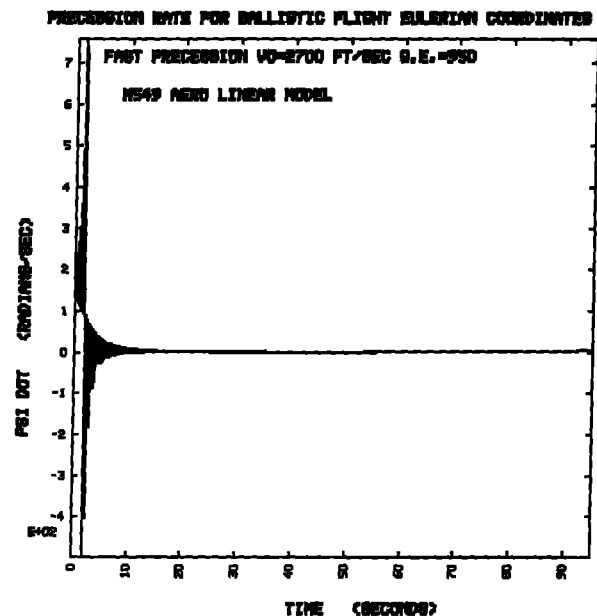


Figure 14.

Table 3. Initial Conditions for Ballistic Trajectory Simulation.

Figures No.	Mach No.	Launch Elevation Angle (Degrees)	Site Elevation (Feet above mean sea level)	Θ (degrees)	$\dot{\Theta}$ (rad/sec)	ϕ (rad/sec)	$\dot{\Psi}$ (rad/sec)	C_{mpu} (model)
12-17	2.5	53	928	10	0.1	1570	200	M549
18-22	0.99	53	928	10	0.1	628	10	M549
23-27	2.5	53	928	10	0.1	1570	200	$0.5 \times$ M549
28-31	0.99	53	928	10	0.1	628	10	$0.5 \times$ M549

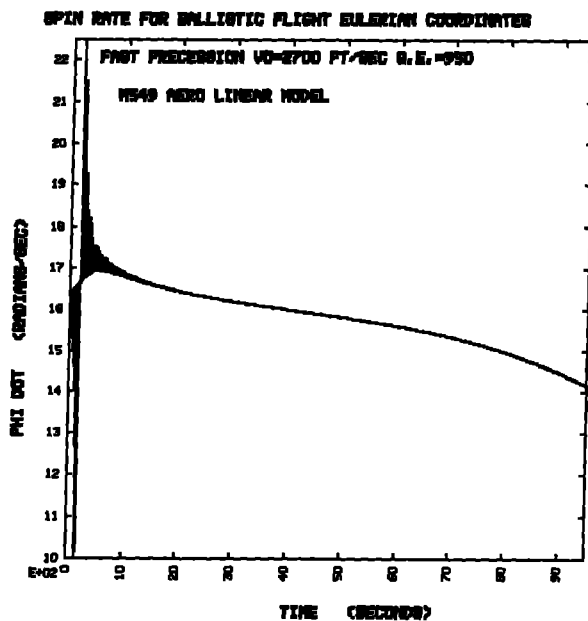


Figure 15.

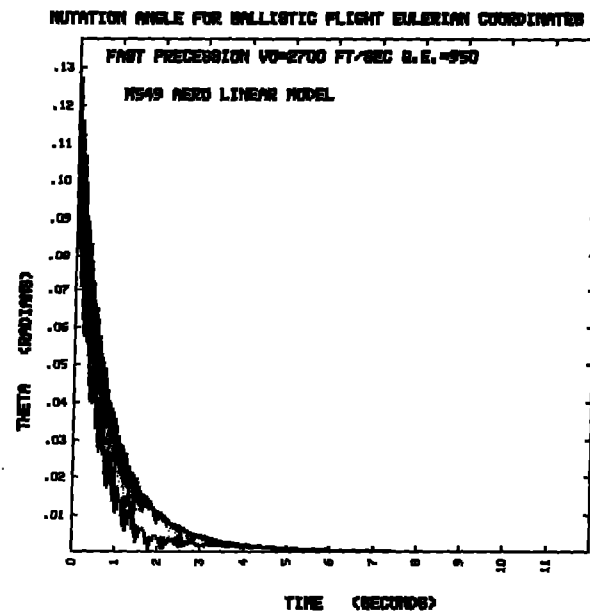


Figure 16.

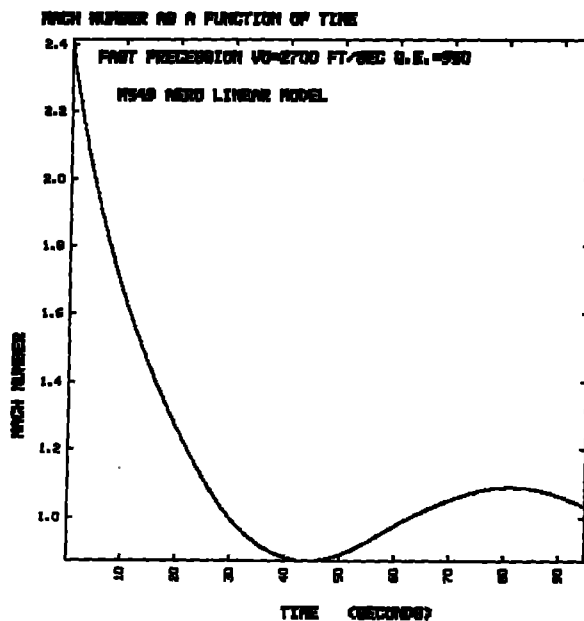


Figure 17.

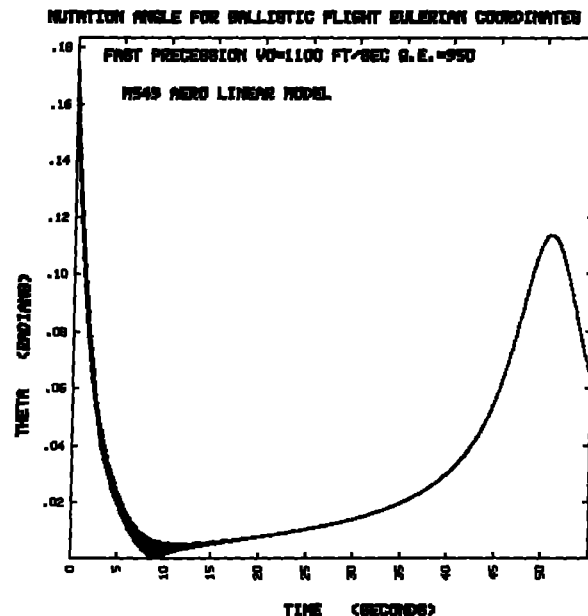


Figure 18.

Results of the transonic simulation are provided in Figs. 18 through 22. Once again, the fast mode was assumed as an initial condition, but the precession rate quickly decayed to the slow mode.

From Fig. 18, it is obvious that the oscillatory damping of the nutation angle is similar to that in Fig. 2. But the actual damping begins long after the onset of Magnus slope coefficient reversal, which, from Fig. 22, occurs at $t = 5.0$ s. Examination of the nutation rate plots of Figs. 15 and 3, however, reveals important differences in the ballistic model and the CDCV model. The damping of nutational oscillations is widely attributed to the nonlinearities in the Magnus velocity profile in the aeroballistic development. Clearly, this cannot explain the features of Fig. 18.

A certain type of M549 has been modified with a new

rotating band. The proposed aerodynamic model for this shell includes a doubling of the Magnus slope coefficient while all other variables are kept approximately the same. A simulation of the modified shell is provided in Figs. 23–27. In these figures, the nutation rate is little affected by the Magnus moment change. But there are subtle differences in the nutation angle. In the expanded time scale of Fig. 27, the oscillatory component is essentially well-damped from $t = 0$ until it disappears. In Fig. 16, the oscillatory envelope showed growth and then subsequent decay between $t = 0$ and $t = 5.0$ s. In Fig. 27, sinusoidal variations decay monotonically. The next most salient feature of the motion is that the fast precession rate remains excited throughout the flight. Oscillations around the precession rate persist, and the beat frequency is clearly present.

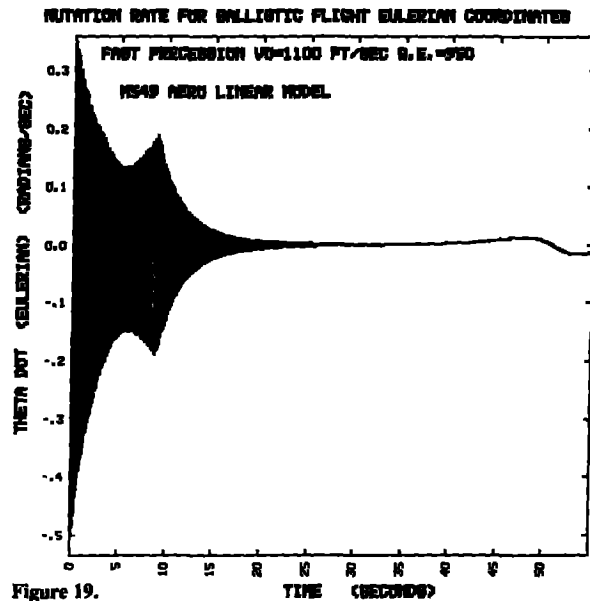


Figure 19.

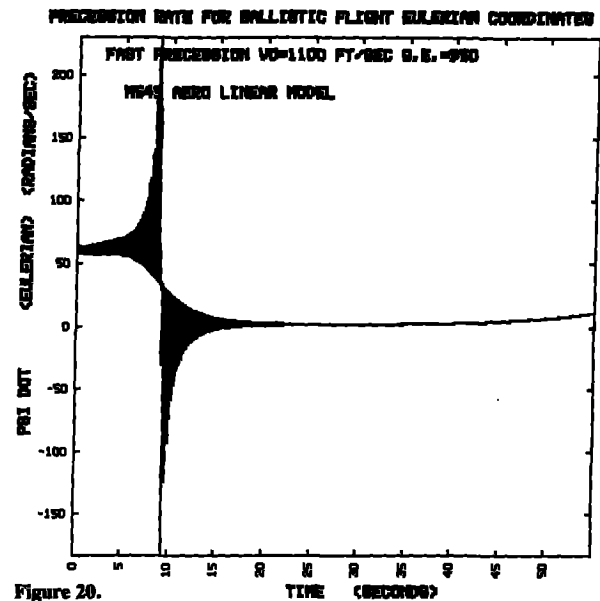


Figure 20.

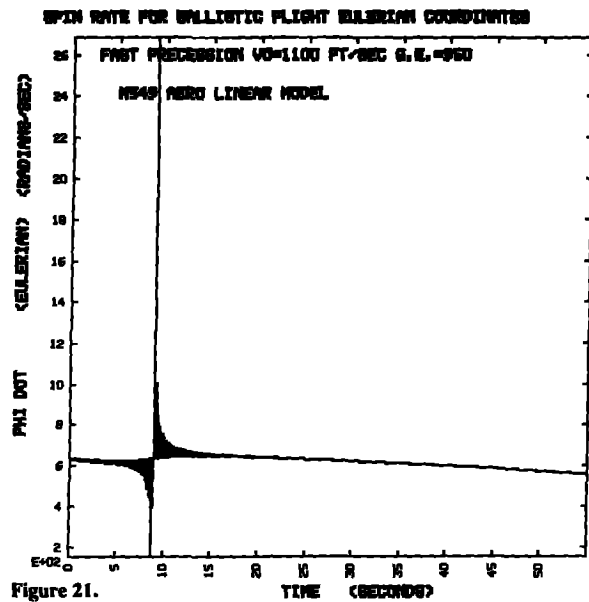


Figure 21.

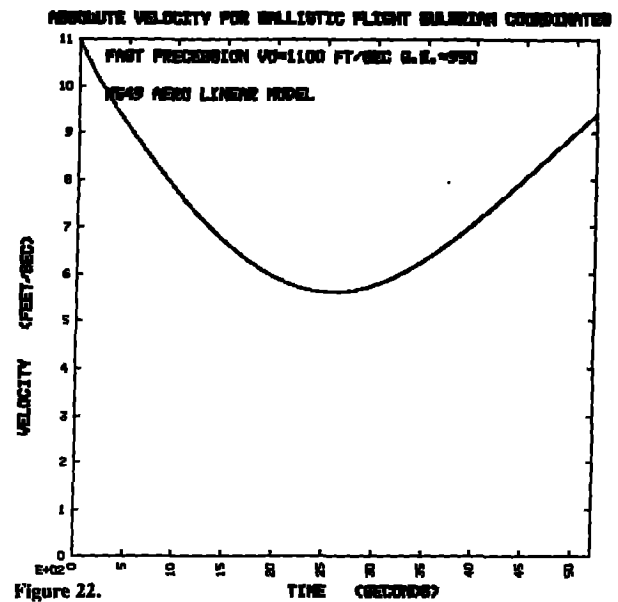


Figure 22.

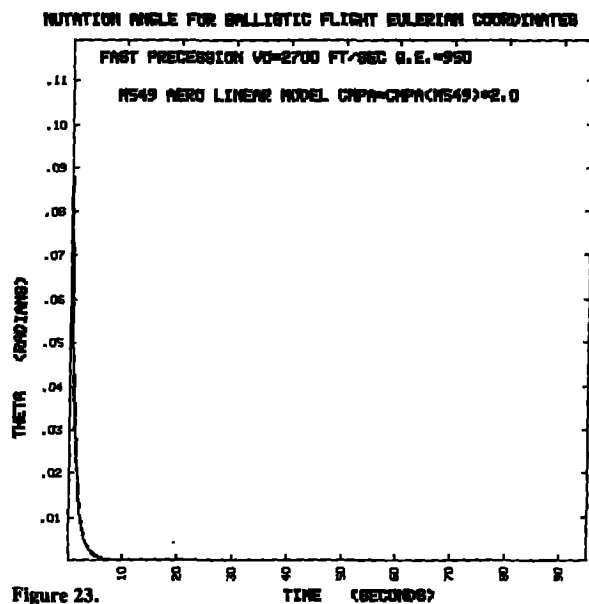


Figure 23.

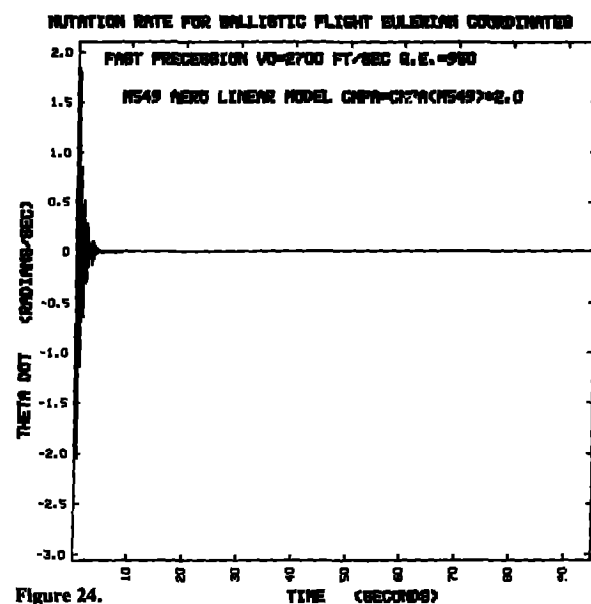
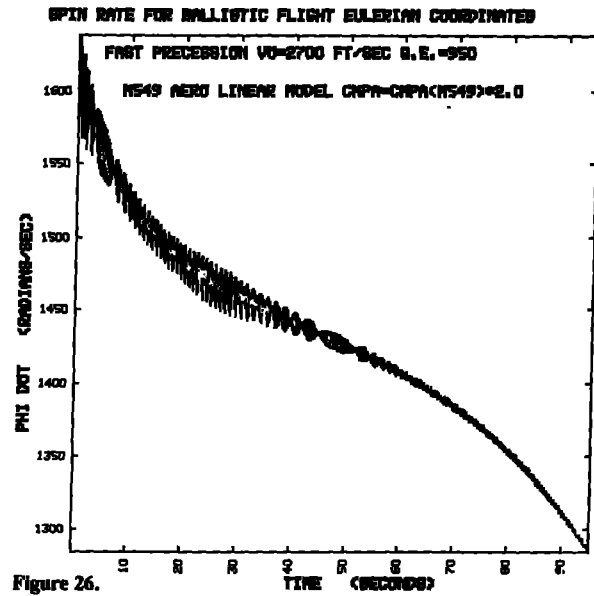
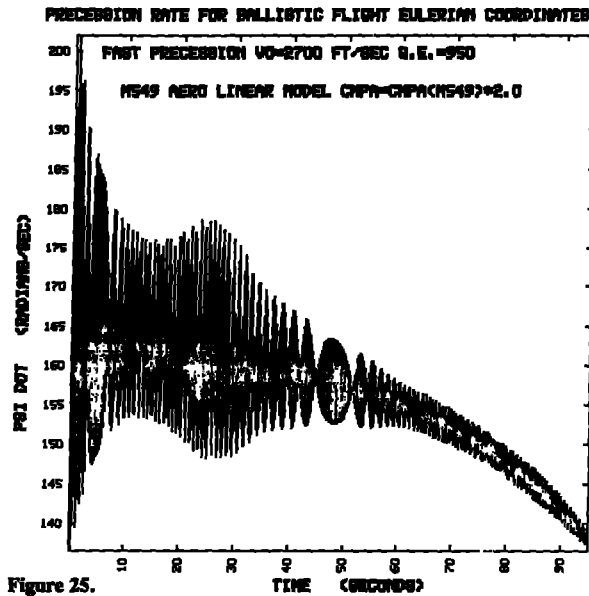
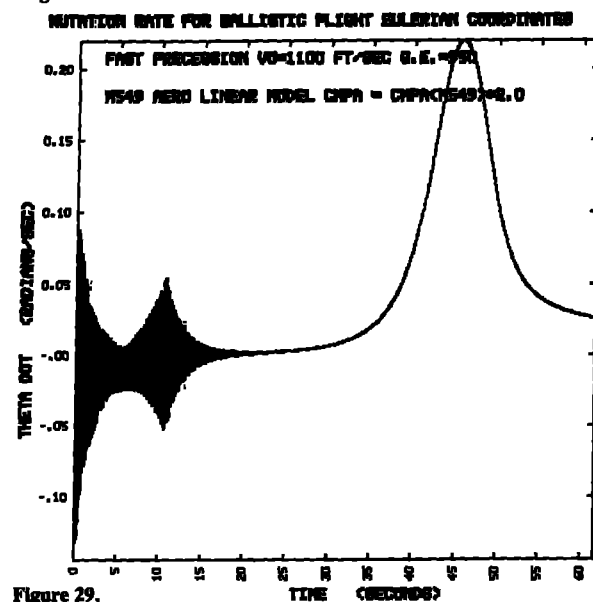
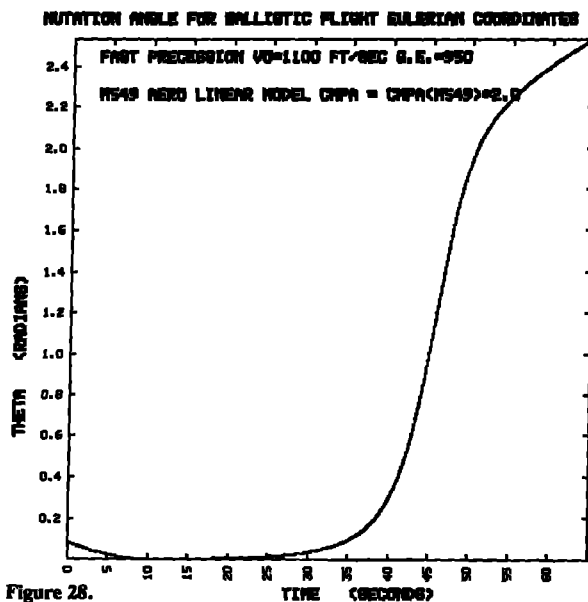
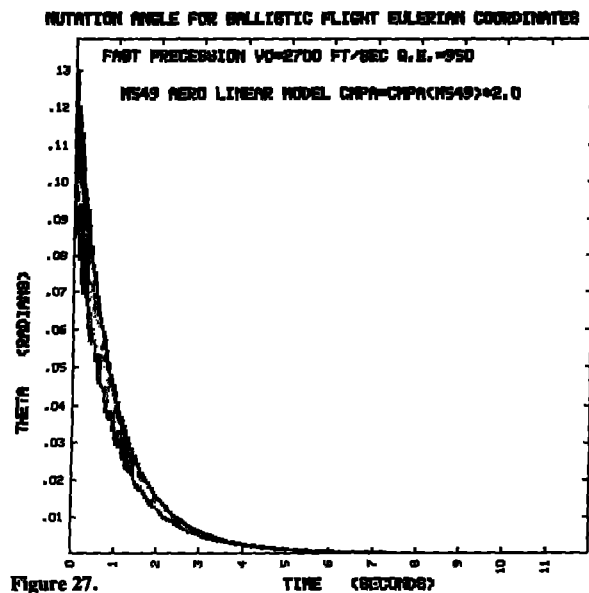


Figure 24.



Utilizing the same model to generate a similar set of plots for transonic flight, one finds an entirely different form of motion. The results are given in Figs. 28-31. Now the nutation grows rapidly after 10 or 15 s. (Beyond a total nutation angle of 20° the results are undoubtedly invalid due to aerodynamic stall, but the integration was allowed to continue to provide an assessment of the rapidity of the angular growth.) Recall that the analytical model describing only the oscillatory portion (up to 16 s) of the flight would not predict this catastrophic growth.



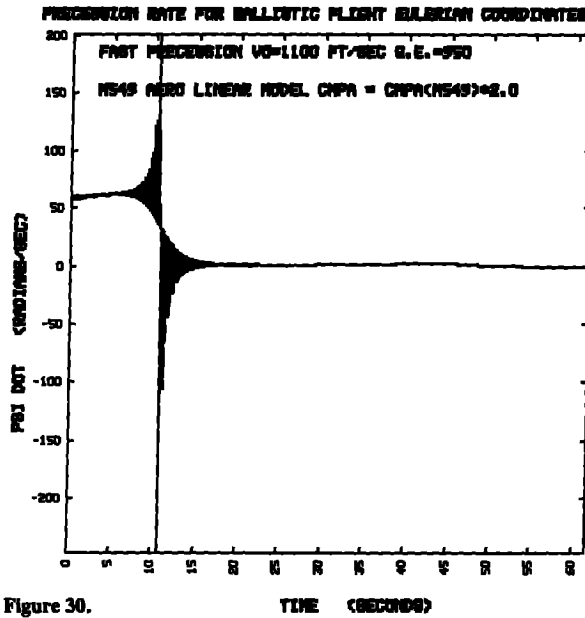


Figure 30.

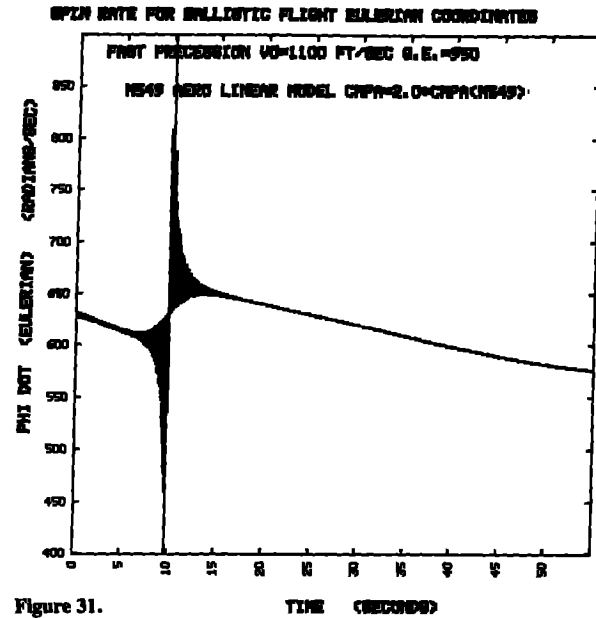


Figure 31.

Experimental Comparison: Gyroscopic Model.

Four projectiles with aerodynamic and mass characteristics considered to be a ballistic match to the M549 were flown with a body coordinate-sensing device known as a "strainsonde".¹⁰ In addition each projectile carried a solar-aspect-angle sensing device called a "yawsonde".¹¹

The initial launch conditions most closely matched those of Figs. 23–27. The strainsonde, as the name implies, was a strain gauge mounted to sense acceleration along the radial axis of a body. No contribution due to longitudinal motion was expected. The strainsonde had a low-end transmission-frequency cutoff of 5 Hz and a upper cutoff of 500 Hz. Signals were transmitted continuously from the time of muzzle exit until ground impact downrange.

As a counterpoint to the strainsonde, the yawsonde recorded motion with respect to *Newtonian*-fixed space (the motion of the sun was assumed to be small during the flight time). If a suitable coordinate transformation exists between the Z-axis of Fig. 1 and the alti-azimuth solar direction vector (this transformation is usually taken to be the vector dot product of the velocity vector and solar direction vector), then any vector expressed in Eulerian space can easily be transformed into Newtonian space, allowing a comparison of yawsonde and strainsonde data.

In this case, the coordinate transformation provides a change of basis for the Eulerian rotation-rate vector. In matrix form,

$$\begin{bmatrix} \omega_{x_N} \\ \omega_{y_N} \\ \omega_{z_N} \end{bmatrix} = \begin{bmatrix} \cos \Psi & -\cos \Theta \sin \Psi & \sin \Theta \sin \Psi \\ \sin \Psi & \cos \Theta \cos \Psi & -\sin \Theta \cos \Psi \\ 0 & \sin \Theta & \cos \Theta \end{bmatrix} \begin{bmatrix} \omega_{x_E} \\ \omega_{y_E} \\ \omega_{z_E} \end{bmatrix} \quad (15)$$

Substituting the angular velocity components in Eulerian vector space, $\omega_{x_E} = \dot{\Theta}$, $\omega_{y_E} = \dot{\Psi} \sin \Theta$, $\omega_{z_E} = \dot{\phi} + \dot{\Psi} \cos \Theta$, into equation (15), one obtains

$$\omega_{x_N} = \dot{\phi} \sin \Theta \sin \Psi + \dot{\Theta} \cos \Psi \quad (16a)$$

$$\omega_{y_N} = -\dot{\phi} \sin \Theta \cos \Psi + \dot{\Theta} \sin \Psi \quad (16b)$$

$$\omega_{z_N} = \dot{\phi} \cos \Theta + \dot{\Psi}. \quad (16c)$$

Figure 32 shows the spectral development during actual flight of various rigid-body excitation modes in body-fixed strainsonde coordinates for one typical shell.¹² Each experimental spectral cut is taken at a 1.6 s time interval commencing simultaneously with gun exit. The resulting three-dimensional presentation is called a "waterfall" plot. Two closely spaced high frequencies, 224 and 251 Hz, predominate at $t=0$. It may seem at first that these frequencies are the spin and fast eigen nutation frequencies because the fast precession frequency and fast eigen nutation frequency are almost identical. Distinguishing one from the other in the spectral record would appear difficult. But if there is any variation in the radius vector from the center of spin to the strain gauge (almost certainly the case except for the highly unlikely possibility that the geometric axes and the principal axes are exactly coincident), then the product of the harmonic precessional variations and the spin modulation will have a frequency of $\dot{\phi} - \dot{\Psi}$. Alternatively, if the strain gauge measured centripetal acceleration modulations due to a change in the radius vector from the precessional center of rotation [$r = \Theta \cdot (z_{c.g.} - z_{s.s.})$], the variations would be the square of the harmonic precessional term, which has spectral content at $2\dot{\Psi}$. Since the second major peak in the data record occurs at $\dot{\phi} - \dot{\Psi}$, it seems likely the second major peak can be associated with precessional motion.

A further corroboration is shown when the Fourier magnitude of the spectral content is examined. In Fig. 32, the magnitude exists almost undiminished throughout the flight at the frequency $\dot{\phi} - \dot{\Psi}$. But the yawsonde record and the numerical simulation both show that the nutational oscillations have damped to zero after 10 s. However, the numerical simulation predicts that precessional oscillations will persist for the entire length of the flight. Close inspection of the waterfall plot shows that a frequency resembling the $2\dot{\Psi}$ frequency appears at first but decays shortly into the trajectory.

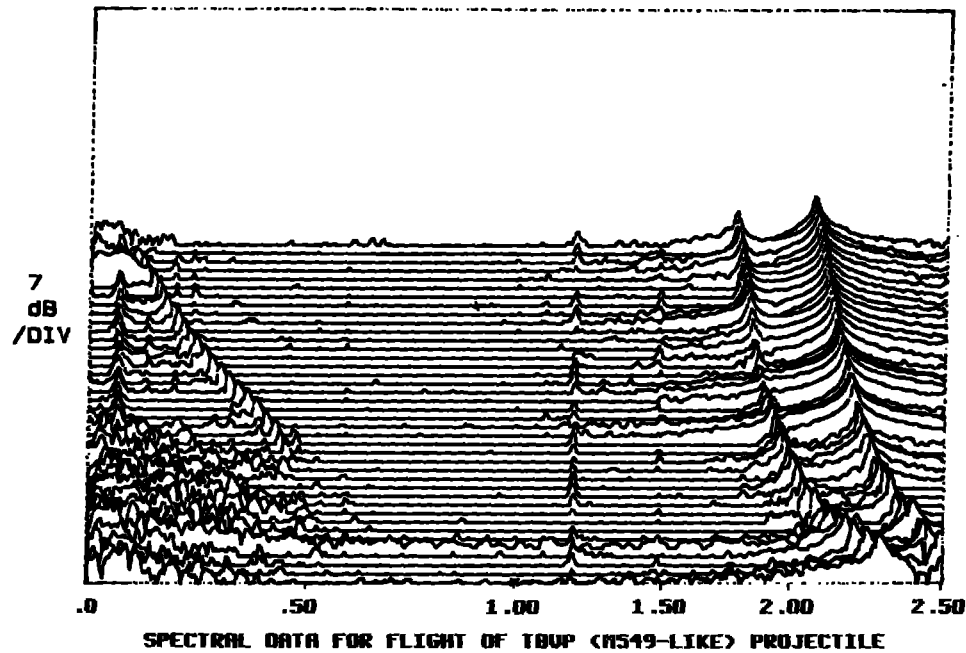


Figure 32.

Figures 33 and 34 are the equivalent yawsonde plots for the same flight. Unfortunately, transmission of data for Figs. 33 and 34 did not begin until several seconds after gun exit, so it is impossible to know the exact initial condition of the projectile. But, from Fig. 34, the total Newtonian spin rate is well above 260 Hz at first transmission and was probably

at least 265 Hz at $t=0$. From the waterfall plot $\dot{\phi}_{t=0} = 251$ Hz and $\dot{\psi}_{t=0} = 24.6$ Hz. Using equation (16c),

$$\dot{\phi}_{\text{NEWT}} = 265 = 251 \cos \Theta_0 + 24.6, \text{ and } \Theta_0 = 15^\circ.$$

This value is not very different than observed values for the initial nutation angle.

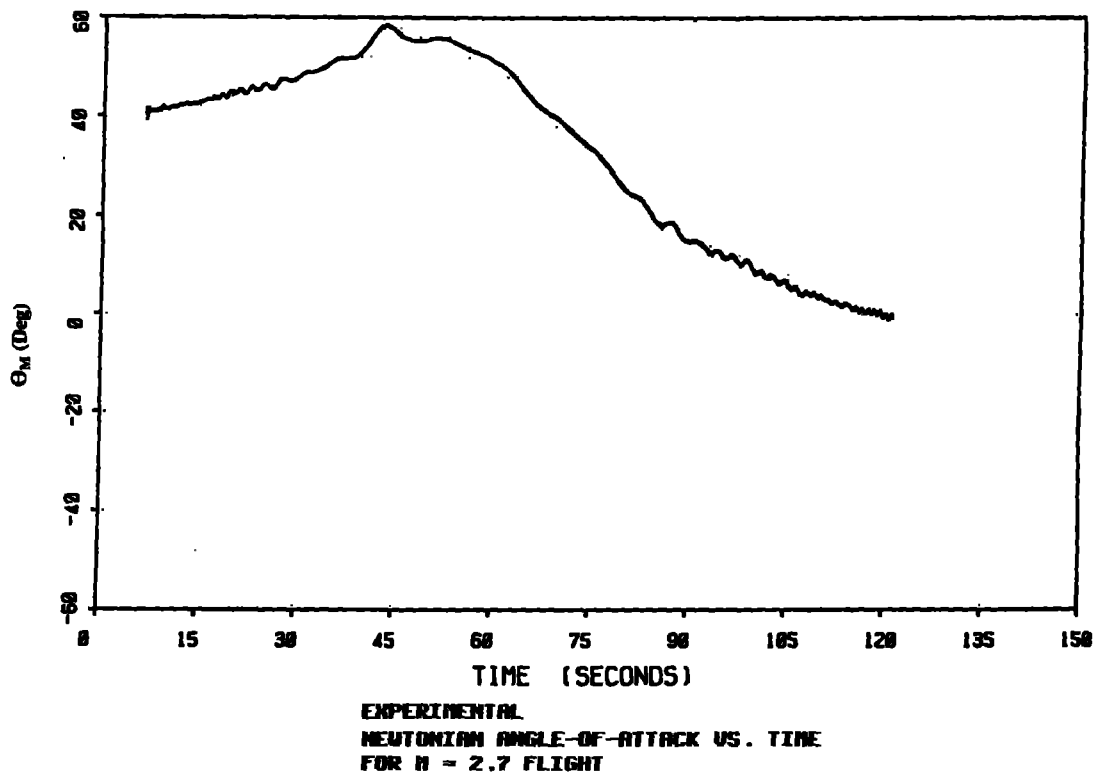
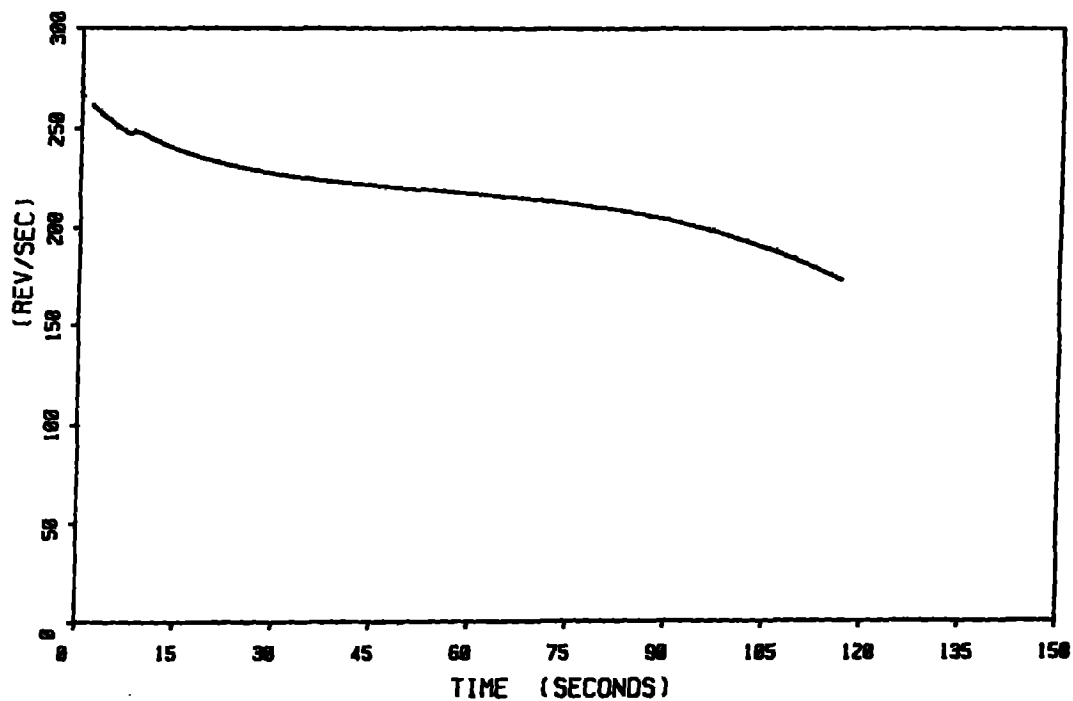


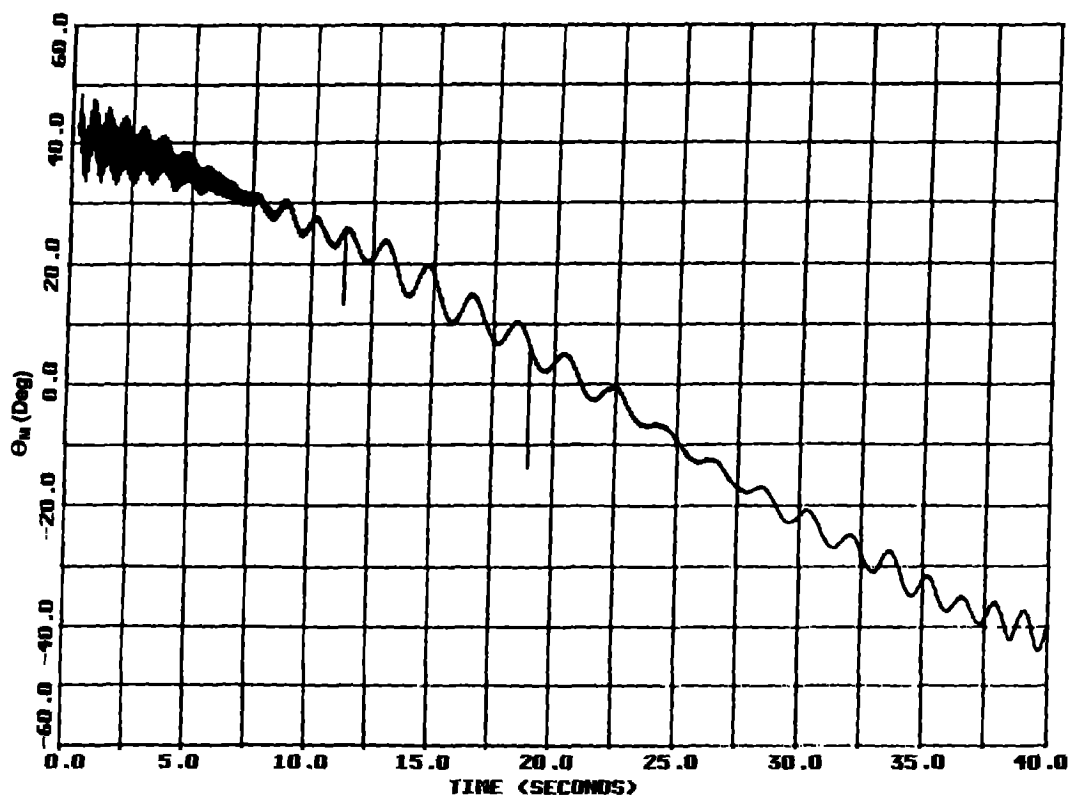
Figure 33.



EXPERIMENTAL
NEWTONIAN SPIN RATE VS. TIME
FOR $M = 2.7$ FLIGHT

Figure 34.

No strainsonde data exist for transonic trajectories, but a number of yawsonde traces are available. Figure 35 is an example of a yawsonde trace in which the initial conditions closely match those of Figs. 18-22.



EXPERIMENTAL NUTATION-TIME HISTORY FOR $M = .99$ FLIGHT

Figure 35.

Figure 36 shows the equivalent simulation analysis transposed into Newtonian vector space by the matrix operation shown in equation (15). A comparison of the two results shows good agreement with the model. (The slow change in the experimental baseline result is due to a continual change in elevation angle as the shell follows its trajectory.)

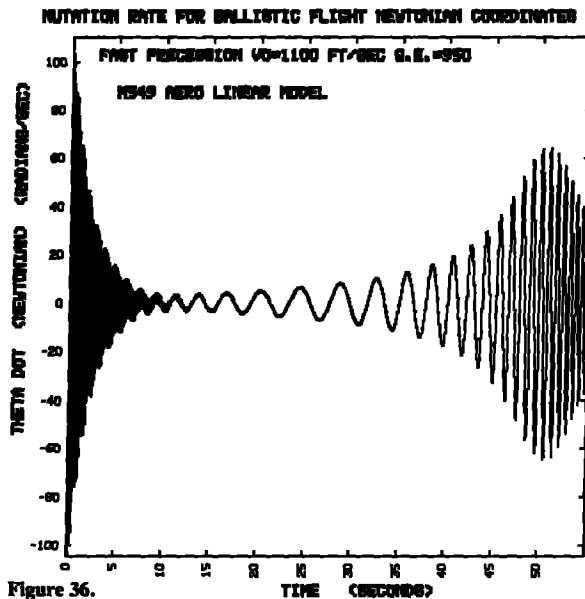


Figure 36.

A reinspection of Figs. 18–22 reveals that the slow frequency oscillation after $t=20$ s is not due to dynamic changes in the nutation angle. Instead, it arises from a recasting of the polar circular coning motion into a rectangular coordinate description. But the state of the coning frequency affects this result in both frequency and limit cycle motion and will change the growth characteristic of the envelope. As an illustration of this point, the Magnus slope coefficient was doubled in the simulation and plotted in Fig. 37. Equivalent Euler space results are those shown in Figs. 28–31. From equation (11c), (the analytical solution), it is not clear that changing the Magnus slope coefficient should change the frequency in any way, but this is exactly the result observed in the simulation.

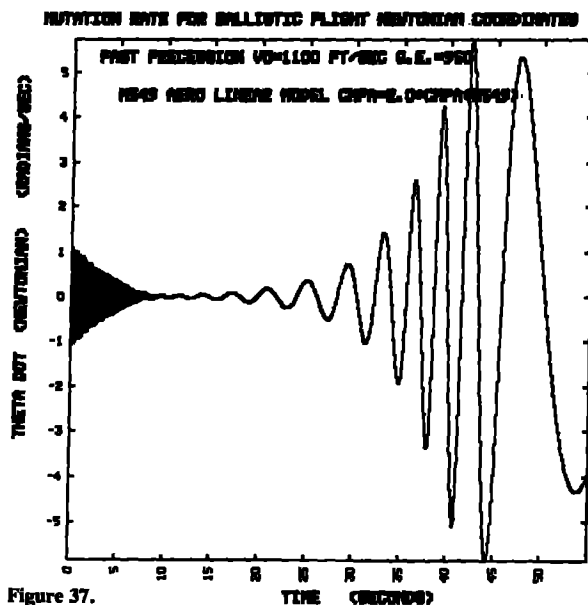


Figure 37.

Conclusions

An alternative to the aeroballistic coordinate description of projectile motion has been provided. When compared with actual flight data, theory and experiment show good agreement. On the other hand, the new results provide explanations for some motions not addressed by the aeroballistic solution and show where the analytical results fail to properly match numerically integrated results.

Acknowledgements

The strainsonde used in the experimental test program was designed, fabricated and tested by Dr. W.P. D'Amico of the U.S. Army Ballistic Research Laboratory. In addition, he provided the reduced data of the results for both the strainsonde and yawsonde graphs used in the text.

The development of this theory has benefitted from conversations with Albert E. Hodapp of Sandia National Laboratories, Albuquerque, New Mexico.

References

1. H. R. Vaughn, *A Detailed Development of the Tricyclic Theory*, Sandia Laboratories, Albuquerque, N.M., SC-M-67-2933 (1968).
2. C. H. Murphy, *Free Flight Motion of Symmetric Missiles*, U.S. Army Ballistic Research Laboratory, Aberdeen Proving Ground, Maryland, 1216-AD442757 (1963).
3. R. H. Whyte and W. H. Mermagen, "A Method for Obtaining Aerodynamic Coefficients from Yawsonde and Radar Data," *AIAA Journal of Spacecraft and Rockets* 10 (6) (1973).
4. A. E. Hodapp, *Equations of Motion for Free-Flight Systems of Rotating-Translating Bodies*, Sandia Laboratories, Albuquerque, N.M., SAND 76-0266 (1976).
5. T. O. Morgan, "The Influence of Internal Moving Parts on the Ballistic Flight Path of a Projectile," in *Proceedings of the 12th Atmospheric Flight Mechanics Conference, Snowmass, Colorado, August 19–21, 1985*, American Institute of Aeronautics and Astronautics, New York, New York (1985).
6. C. H. Murphy, "Influence of Moving Internal Parts on Angular Motion of Spinning Projectiles," *Journal of Guidance and Control* 1 (2), 117–122 (1978).
7. A. E. Hodapp, *Effect of Mass Asymmetry on Ballistic Match of Projectiles*, Sandia National Laboratories, Albuquerque, N.M., SAND77-0324 (1977).
8. H. Goldstein, *Classical Mechanics*, (Addison-Wesley Publishing Co. Inc., Reading, Mass. 1950).
9. A. Hindmarsh, *LSODE: The Livermore Solver for Ordinary Differential Equations*.
10. W. H. Clay, *A Strain-Sonde Technique for the Measurement of Mechanical Time-Delay Fuze Functions and Performance*, U.S. Army Ballistic Research Laboratory, Aberdeen Proving Ground, Maryland, BRLMRPT. ABRL-MR-03309 (1983).
11. W. H. Mermagen, *The Design of a Second Generation Yaw Sonde*, U.S. Army Ballistic Research Laboratory, Aberdeen Proving Ground, Maryland, BRLMRPT. ABRL-MR-2368 (1974).
12. W. P. D'Amico, *In-Flight Yaw and Vibration Data for the 155 mm Joint Ballistic Test Projectile with Propelling Charge M203 and Rocket-On*, U.S. Army Ballistic Research Laboratory, Aberdeen Proving Ground, Maryland, BRL-IMR-826 (1984).